In Situ Digital Image Correlation Observations of Laser Forming

Fidder, Herman; Admiraal, Joris P.J.; Ocelík, Václav; De Hosson, Jeff Th M.

Published in:
Metals

DOI:
10.3390/met10010017

Publication date:
2020

metals

MDPI

Article

In Situ Digital Image Correlation Observations of Laser Forming

Herman Fidder [1,2,*], Joris P. J. Admiraal [1], Václav Ocelík [1] and Jeff Th. M. De Hosson [1,*]

[1] Department of Applied Physics, Zernike Institute for Advanced Materials, University of Groningen, 9747AG Groningen, The Netherlands
[2] Department of Mechanical Engineering, Cape Peninsula University of Technology, Cape Town 7535, South Africa
* Correspondence: H.Fidder@rug.nl (H.F.); j.t.m.de.hosson@rug.nl (J.T.M.D.H.)

Received: 10 November 2019; Accepted: 17 December 2019; Published: 21 December 2019

Abstract: In this study experimental and modelling methods are used to examine the microstructural and bending responses of laser-formed commercially pure titanium grade 2. The in situ bending angle response is measured for different processing parameters utilizing 3D digital image correlation. The microstructural changes are observed using electron backscatter diffraction. Finite element modelling is used to analyse the heat transfer and temperature field inside the material. It has been proven that the laser bending process is not only controlled by processing parameters such as laser power and laser beam scanning speed, but also by surface absorption. Grain size appears to have no influence on the final bending angle, however, sandblasted samples showed a considerably higher final bending angle. Experimental and simulation results suggest that the laser power has a larger influence on the final bending angle than that of the laser transverse speed. The microstructure of the laser heat-affected zone consists of small refined grains at the top layer followed by large elongated grains. Deformation mechanisms such as slip and twinning were observed in the heat-affected zone, where their distribution depends on particular processing parameters.

Keywords: EBSD; DIC; laser forming; plastic deformation; HCP interaction

1. Introduction

Laser forming (LF) was first reported in the 1980s within the ship building industry using flat steel plates which has been formed into three-dimensional shapes as reported by [1,2]. It was also further reported that laser forming can advocate as a highly versatile tool for a broad range of material processing applications. LF is a contactless method of producing controlled deformation of metallic and non-metallic structures by introducing laser energy at specific parameters as stated by [3,4]. LF can be described as a process in which thermal stress is introduced into the substrate structure by means of a laser beam. This results in quick local heating without melting. Thermo-elastic plastic distortions will occur because of the onset of thermal stresses (temperature and geometry dependent) exceeding the yield elastic limit (temperature dependent) of the substrate material. The laser is then switched off or shifted in a specific pre-determined pattern which plays an important role in the final shape that will result after cooling. The cooling will lead to the start of bending or shape change of the material substrate. The three bending mechanisms that are associated with LF are the temperature gradient mechanism (TGM), the buckling mechanism (BM), and the shortening or upsetting mechanism (UM) as proposed by [5,6]. In this study the TGM will be dominant since the substrate is considered to be a thick plate i.e., because of the ratio between thickness of the substrate and the depth of laser beam heat affected material. Furthermore, laser forming has numerous processing parameters such as transverse speed, laser beam diameter, distribution of power density (for example TEM_{01}) and wavelength. The

physical properties of the material and surface such as the absorption coefficient, crystallographic orientation, thermal conductivity and thermal expansion also play a vital role in the final desired shape of any material that will undergo LF. The selection of the above-mentioned processing parameters are therefore crucial as previously reported by [7,8]. More recent studies deal with laser forming involving, e.g., the edge effect [9], three dimensional laser forming [10,11] and modelling of multiple scans [12]. However, these studies fall beyond the scope of the current investigation.

A two-layer TGM model has been used in numerous comparative studies as stated by [3]. There are also a number of analytical models available as given by [4,5,13] that have been developed to describe and expand on the main LF mechanisms associated with the TGM. The analytical bending angle model of [4] assumes a delivered energy approach to the temperature field and results in the following formula for the final bending angle:

$$\alpha = \frac{3\,\alpha_{th}\,P\,A}{\rho\,C_p\,v\,s^2} \tag{1}$$

where α_{th} is the coefficient of thermal expansion, P is the laser power, A is the surface absorption coefficient, ρ is the material density, C_p is its specific heat capacity, v is the scanning speed or beam scanning velocity and s is the sample thickness. The model was extended by [14] to include the counter-bending effect in order to account for some of the purely elastic straining. The modified Vollertsen equation for the bending angle as proposed by [14] is

$$\alpha = \frac{21\,\alpha_{th}\,P\,A}{2\,\rho\,C_p\,v\,s^2} - \frac{36\,L\,Y}{s\,E} \tag{2}$$

where L is the half length of the laser track, Y is the yield stress and E is Young's modulus. When comparing Equation (1) with Equation (2), it is clear that the solution includes some material and geometrical parameters to calculate the bending angle. The bending model of [5] only takes into account laser power, sample thickness and beam scanning velocity. The model of [13] additionally takes into account the flow stress at the heated region as variable with the entire equation appearing as a cube root.

Both above mentioned approaches deal with the final bending angle observed after processing by a laser beam. However, for a better understanding, the flow of the thermal strain created during the LF process, which is driven by the TGM, a digital image correlation technique (DIC) [15] could be applied in situ to characterise the movement made by the specimen during processing. Emphasis may be placed on any disordered movement and torsional moments that may lead to an offset when compared to the initial stage. An advantage of DIC is that it can also be used to evaluate any sudden movement during the heating and cooling period. Furthermore, commercially pure (CP) titanium (Ti) experiences an allotropic phase transformation throughout the LF process as the material is heated above the alpha to beta region which is associated with a volume change and therefore influencing the LF process as reported by [8]. This phase transformation always needs to be taken into account when laser processing of Ti or its alloys is studied [13–15]. It is shown in [16] that changes in the deformation bending angles of up to 0.1° can occur in steel when the phase changes from ferrite to austenite. This phase transformation and all other microstructural changes developed during the LF process can be characterized with the aid of electron back-scatter diffraction (EBSD) when considering crystallographic properties of the laser heat-affected zone (LHAZ) within the specimen. The study of [17] showed that the global relieved residual stresses can be ~25% higher for the LF process when compared to that of the traditional mechanical forming process. In addition, local microscopic deformation resolved stress within CP Ti can be as high as ~−180 MPa [18].

The novelty here lies in using in situ DIC equipment that can be used to visualize the bending angle response (e.g., counter bending, buckling, etc.,) in real time when executing laser forming. Furthermore, the bending response can be linked to the microstructural changes (i.e., allotropic phase

transformation, grain growth, grain misorientation changes, etc., via EBSD) within each sample that was subject to specific laser processing conditions. Furthermore, the microstructural changes can give an indication of how the flow of thermal strain was created during the laser forming process which can also be linked to the final temperature distribution within the sample. According to the knowledge of the authors, the combined above-mentioned techniques and direct experimental link between bending angle and microstructural changes have not been performed elsewhere in the literature. More specifically, the bending angle response behaviour will be compared for different processing parameters and different grain sizes. The surface roughness will also be altered in order to investigate the influence of an increased absorptivity coefficient because of surface sandblasting. These observations provide additional insight to the semi-empirical and analytical modelling of LF.

2. Setup—Method

The laser used for the laser forming process is a 3 kW Yt:YAG continuous fibre laser from IPG Photonics. The laser optics with 120 mm focal length is set to a distance of +35 mm out of the focus position, resulting in a laser beam radius of about 2.8 mm, with a Gaussian intensity distribution. Argon shielding gas flow of 15 L/min, positioned approximately 45 mm from the sample, is used to prevent any influence of oxidation on the surface during the laser forming process. The CP Ti sample is fixed with multiple clamps on one side, while leaving the other side free to move, as displayed in Figure 1. The specimen with dimensions of approximately 200 mm in length, 50 mm in width and 3 mm in thickness is raised about 1 mm at the side of the clamps to avoid contact with the aluminium base to prevent any heat transfer. This is shown in Figure 1 together with track 1 being the first laser track, 2 the second, up to the nth laser track. Because of the fact that the plate is fixed on one side parallel to the aluminium base C (see Figure 1) and bending occurred along the axis located inside the laser track, only the free end of the plate is moving, i.e., increasing the detected angle α between side of the plate and horizontal line marked on the base C. The laser beam is scanning the plate surface along the X direction and the centre of the beam is shifted 6 mm in the Y direction between every single laser track, starting with the first laser track about 50 to 60 mm from the free end of the sample. Therefore, the surface heated by the laser is always on the same XY plane at the start of every individual laser track.

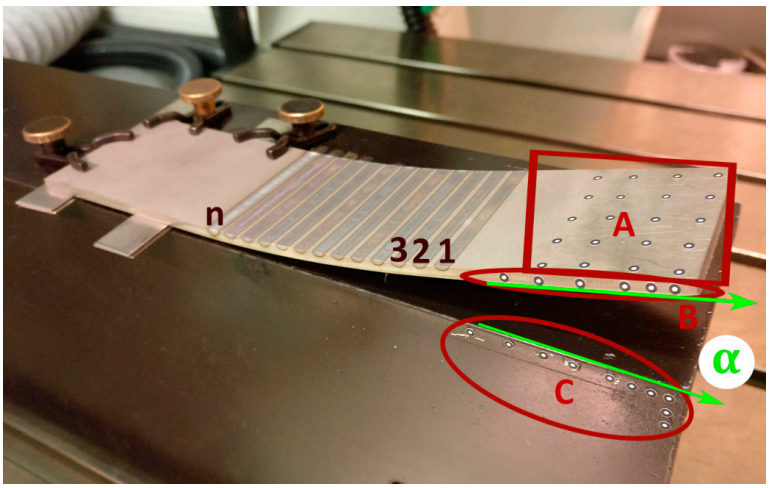

Figure 1. Experimental setup for digital image correlation (DIC) observation of laser forming sample with tracking markers for in-situ measurements on the top (A) and side (B) of the sample and on the base (C). The laser processing sequence in the X direction starts behind the markers; track #1 is followed by the second and third tracks until track n is reached, towards the fixed end. The angle α is the cumulative bending angle between the side sample markers line (B) and the base markers line (C). Spacers were placed below the sample at the fixed end on the left-hand side to minimise any direct heat conduction from the sample into the base.

The bending angle for each individual track i as a function of processing time is therefore given by:

$$\alpha_i\,(t) = \alpha(t) - \sum_{k=0}^{i-1} \alpha_k^f \tag{3}$$

where $\alpha(t)$ is an instantaneous bending angle value observed during the DIC experiment, and the second term represents the accumulated final bending angle because of laser processing of all the previously processed laser tracks.

The DIC setup used for the in situ measuring of the bending angle is a commercially available DIC-Aramis system from GOM mbH, Germany. It is equipped with two 4 MP cameras with a resolution capability of 2400 × 1728 pixels per camera. For optimal lighting conditions, with a high intensity and contrast, two special blue lights are used. This blue light also enables the software to filter interfering ambient light and possible reflections from the laser surface processing. The frame rate used during the in situ experiments ranged from 30 to 60 frames per second (fps). The total number of frames per track varied between 500 and 1500, depending on the scanning speed of the laser beam and the DIC frame rate. The DIC cameras were arranged in such a way that the processing laser track was always out of their field of view in order to avoid any direct beam reflection.

The samples used in the laser forming experiments are all of CP Ti grade 2. During the laser forming process, five parameters are varied namely; transverse speed, power of the laser beam, multiple 100% overlapping laser scans, grain size, and the surface roughness. The laser scanning speed varied between 20, 15 and 10 mm/s, with a range of laser powers depending on the speed, as summarized in Table 1. This table shows only a part of the entire experimental study. Some experiments were repeated 5–6 times with the same laser power and laser scanning speed to estimate the variation in the final bending angle with position on the sample. The range of the laser power varied from the lowest possible setting, i.e., 400 W, which would still result in bending but with minimal effect on the microstructure or LHAZ. The highest possible power setting used was ~1000 W before the onset of melting of the surface. Other processing parameters such as scanning speed and beam diameter have been selected to achieve TGM conditions in all experiments. By repeating the same power, scanning speed and Y starting position settings, multiple scans with 100% track overlapping was achieved while waiting approximately 5 min for the specimen to cool down to room temperature before initiating the next overlap scan.

The influence of the grain size was tested by comparing the response of the as-received and grain grown samples during the LF process to the overall bending angle. The grain grown samples were prepared by heat-treating them for 120 h at ~830 °C i.e., just before the onset of the allotropic phase transformation to achieve the biggest possible grain sizes. Finally, the influence of an increased absorption coefficient was tested by lightly and evenly sandblasting the surface of the specimen to promote better coupling of the laser radiation into the material.

CP Ti specimens were prepared for EBSD analysis as described by [8] using the same field emission gun, EBSD camera, EBSD data analysed software techniques and acceleration voltage to determine the crystallographic orientations. A step size of 0.7 μm and hexagonal grid was used for measurements. During this EBSD data cleaning procedure, crystallographic orientation of no more than 2% of all scanned points has been modified.

In order to simulate the heating of the CP Ti grade 2 metal sheet with a laser beam (as heating source), a time-dependent 3D model was used in the FEM (finite element method) COMSOL Multiphysics® model. The dimensions of the samples used in the model were 200 mm × 50 mm × 3 mm and a Gaussian laser power density distribution (radius of 2.8 mm) was selected. CP Ti grade 2 material properties were used. For simulation of the laser heating model the COMSOL "Heat transfer in solids" package was used, which includes computation of the heat conduction, convective heat flux and general inward heat flux. The mesh used for the laser heating model was substantially refined in the area of the laser track. The model has 76,005 degrees of freedom (+21,662 internal). The model is solved for a time range depending on the laser beam speed, with a step size of 0.01 s. The processing

time of the model was between 6 and 10 min on a standard PC. There was only one calibration constant in the FEM calculation which is the laser beam absorption coefficient. It was empirically calibrated with the experimental data by observing the first melting features in the centre of the laser track.

Table 1. Variation of power, scanning speed, final bending angle and experimental error for individual laser scans on 3-mm thick commercially pure (CP) Ti samples. The track names are formulated by the first scanning speed followed by the laser power.

Track Name	Laser Power (W)	Laser Speed (mm/s)	Bending Angle (Degree)	Experimental Error (Degree)
20/1100	1100	20	1.25	0.01
20/1060	1060	20	1.29	0.02
20/1000	1000	20	1.29	0.02
20/940	940	20	1.18	0.04
20/880	880	20	1.13	0.04
20/820	820	20	1.09	0.04
20/760	760	20	0.94	0.04
20/680	680	20	0.84	0.03
20/620	620	20	0.83	0.03
20/560	560	20	0.67	0.01
20/500	500	20	0.46	0.02
20/720	720	20	0.84	0.03
20/1300	1300	20	1.39	0.03
20/1400	1400	20	1.52	0.02
10/580	580	10	0.96	0.01
10/580	580	10	1.10	0.01
10/550	550	10	1.05	0.02
10/530	530	10	0.96	0.01
10/500	500	10	0.87	0.01
10/470	470	10	0.76	0.01
10/440	440	10	0.66	0.01
10/410	410	10	0.54	0.02
10/380	380	10	0.33	0.02
15/795	795	15	0.99	0.01
15/705	705	15	1.00	0.01
15/615	615	15	0.82	0.01
15/570	570	15	0.69	0.02
15/510	510	15	0.44	0.01
15/420	420	15	0.23	0.02

3. Experimental Results

Table 1 shows the range of bending angle dependence with respect to laser powers and scanning speed, which varied between 20, 15, and 10 mm/s, with an experimental error estimated from the final bending angle noise ranging from 0.01° to 0.04°. By repeating the experiments (5–6 times) with the same laser power and scanning speed, standard deviations not exceeding 10% of the final bending angle were obtained.

The movement of the markers placed on the sample and basement during laser forming is recorded in situ as illustrated on a single frame image in Figure 2, which is at the free end of the sample. An overlay is constructed with the ARAMIS software (v. 2017, GOM mbH, Braunschweig, Germany) containing the lines and angles of interest that are pre-defined from the markers. Line 1 and Line 2 are used to construct Angle 1, which is used to measure the overall bending angle from the first frame until the last frame (first/reference frame vs. last frame). Also, Lines 3, 4 and 5 are used to inspect any torsional effect during the LF process by comparing them to one another i.e., Angle 2 vs. Angle 3 vs. Angle 4. It has been observed in all experiments that there was no difference in time response for all four pre-defined bending angles. The bending response is uniform over the whole width of the

specimen during the LF process and no variances are seen for the final bending angle, therefore no torsional effect is encountered.

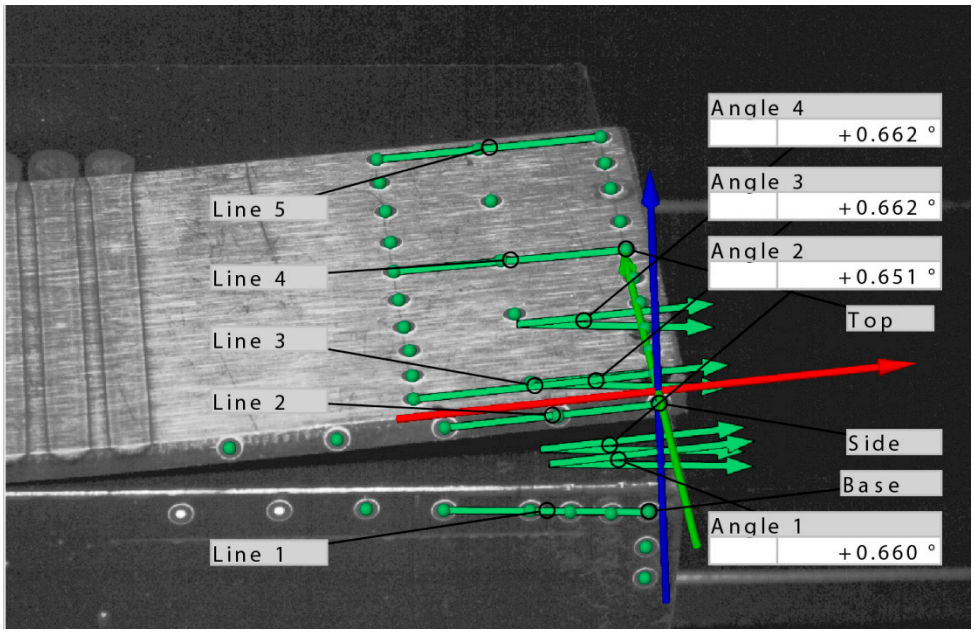

Figure 2. Aramis DIC software representing a single left charge couple device camera frame collected during the in-situ measurement. An overlay containing the calculated angles with respect to the markers are shown.

Figure 3 shows the bending angle response of three different samples and different LF processing conditions. At the beginning of each experiment the bending angle is close to zero with a noise of about 0.01°. DIC also registers small vibrations at the instant when the laser head mechanism starts to move towards the sample. At the moment when the beam hits the sample edge, the sample starts to bend with almost a constant bending rate. Furthermore, it was observed during the bending angle response that a small amount of counter bending is present with the onset of the laser beam onto the sample. However, the data recorded in this study shows that the counter bending is not an important factor during the LF process for a 3-mm thick plate. This bending rate depends on the laser beam power and transverse speed. Close to the end of the bending process, just before the laser beam leaves the sample (between region 2 to 3 in Figure 3), the bending rate is increased for a short period of time. The entire bending process of the sample stops instantaneously when the laser beam moves off the sample. The bending angle maintains a constant value over time which includes some vibration effects because of the three axis machine movements. The vibrations are represented by small valleys and peaks during region 1 and 3. Figure 3 clearly demonstrates that each combination of processing parameters results in a different final bending angle measured with an experimental error of approximately 0.01–0.04° as indicated in Table 1. For a better understanding why the bending rate changes its value, the derivative of the bending angle with respect to time of sample 15/570 shown in Figure 3 is plotted in Figure 4. The bending response starts with a small amount of counter bending as predicted by [19], followed immediately by positive bending at a constant speed (region 1 to 2 in Figure 4). When the laser beam moves onto the edge of the sample, the bending response accelerates (region 2 to 3 in Figure 4). Studying this behaviour for all possible combinations of processing parameters leads to the conclusion that bending acceleration occurs when the laser beam approaches the end edge of the sample, where heat removal is restricted and the temperature inside the processing zone within the material is higher. The increase in bending response directly after region 1 is attributed to the rise in temperature from room conditions, which indicates the onset of the flow of thermal strain.

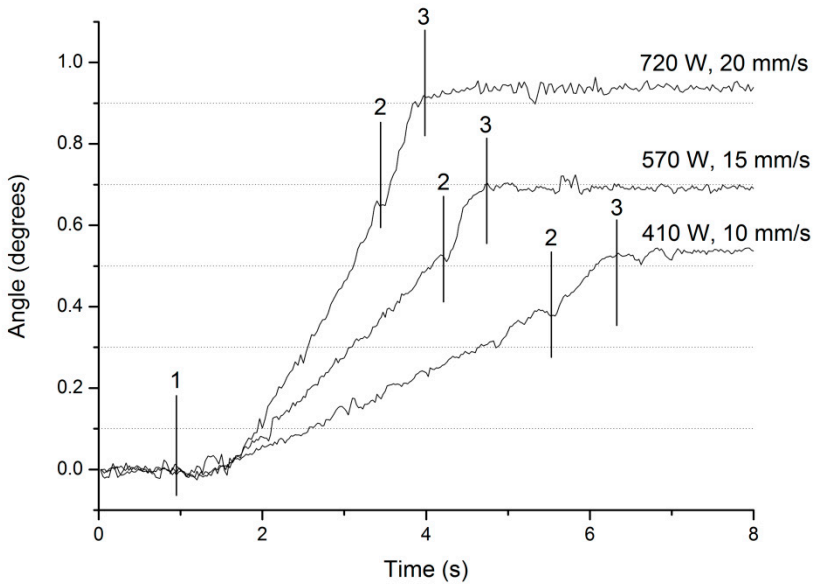

Figure 3. Bending angle detected in situ by DIC for three different processing conditions. Two distinct behaviours can be seen with respect to the slope of the bending angle in region 1 to 2 and region 2 to 3.

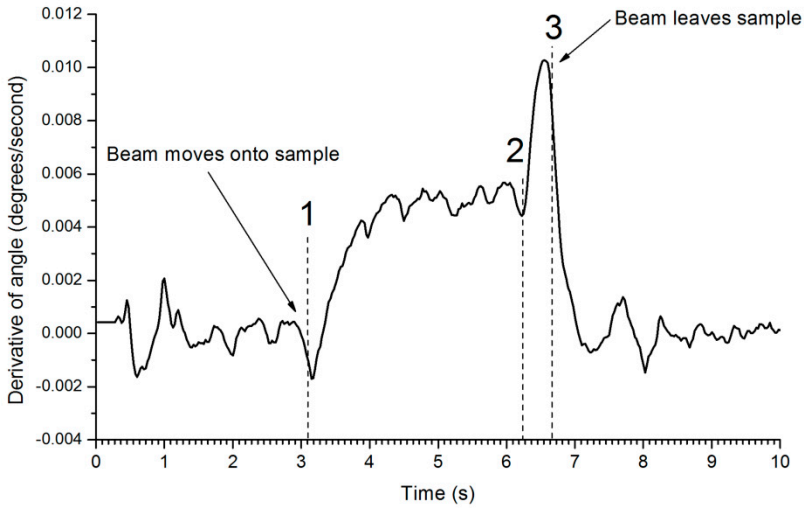

Figure 4. The derivative of the bending angle with respect to time on sample 15/570 from Figure 3 is depicted. The bending response starts with a small amount of bending in the $-Z$ direction, as predicted by theory, followed immediately by bending with a constant speed in the $+Z$ direction (region 1 to 2). At the moment the laser beam moves onto the edge of the sample, the bending response accelerates.

The mechanisms by which process parameters and plate thickness affect the bending angle during the LF process are similar to that of flame heating and arc welding as described by [2]. As a result thereof, the primary factors in LF are laser power (P), scanning speed (v) and plate thickness (s). If only the laser parameters P and v would be varied in Equations (1) and (2), the size of the final bending angle should be, according to these models, linearly proportional to the ratio P/v, referred to as the line energy because of its dimension (J/m) [20].

To compare the measurements for different values of laser power and transverse speed, the bending angle versus the line energy is presented in Figure 5. One can clearly see that for the same transverse speed the final bending angle increases almost linearly with increasing line energy (the three surface melting data points for the 20 mm/s scanning speed should not be considered). However, the laser bending angle in experiments with higher scanning speeds, results in a higher final bending angle for the same line energy, which is in contrast to the model proposed by Vollertsen (Equation (1)).

The final bending angle does not scale with the line energy parameter. Figure 5 also illustrates that for each scanning speed there exists a slightly different interval of line energies resulting in a detectable laser bending angle without surface melting.

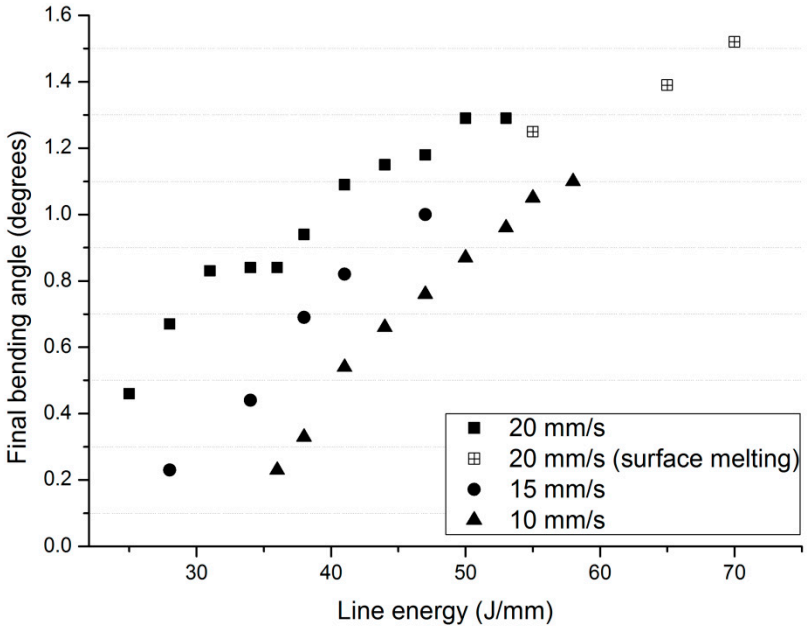

Figure 5. Final bending angle versus line energy (P/v) for scanning speeds of 20, 15 and 10 mm/s. For every individual transverse speed, the bending angle is almost linearly dependent on the laser power.

Figure 6 shows the successive bending angle response of different tracks with multiple overlapping scans using three different laser powers (580 W, 500 W and 410 W) at the same scanning speed of 10 mm/s. This was achieved by starting at the same Y position and scanning the same line multiples times. A single line was scanned six times (100% overlap) while waiting about 5 min to ensure that the sample is again at room temperature before starting the consecutive scan. All samples showed an increase in bending angle response for the second track, which after the response slowly decreases in the following tracks and tends towards an asymptotic bending angle value. The bending response shows good repeatability as it achieved almost identical values measured on two different samples using the same laser power of 410 W.

The effects of an increase in absorptivity (by means of sandblasting the samples lightly) and grain size are shown in Figure 7. Three samples, as-received, as-received with sandblasted surface and grown grains and sandblasted surface, were all laser formed with a fixed scanning speed of 15 mm/s. For the as-received and big grain, sandblasted samples the laser power was varied but not for the as-received, sandblasted sample. Three different as-received sandblasted samples were tested for repeatability thus yielding similar data points. The big grains plus sandblasted samples show a significant increase in final bending angle when compared to the non-sandblasted as-received sample, especially for lower laser powers. The as-received sandblasted samples show a similar final bending angle when compared to the grain grown sandblasted sample tested at the same laser power. This implies that the absorption coefficient is a more important factor for the bending angle response, while the grain size has only a small influence. One of the reasons to study the grain grown sample was to see whether the allotropic phase transformation may amplify the bending during the LF process and if it could be detected by the DIC recording.

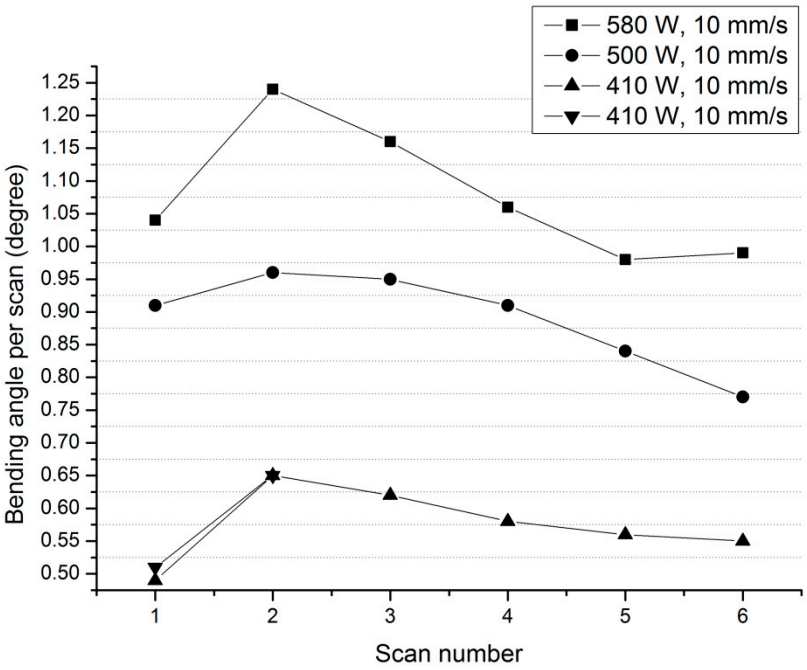

Figure 6. Bending angle response of multiple overlapping tracks using three different laser powers at the same scanning speed. The total bending angle (i.e., the sum off bending angles in 6th and all previous scans) after the 6th scan for the 580 W, 500 W and 410 W is 6.46°, 5.34° and 3.45°, respectively. The total bending angle after the 2nd scan (sum of bending angle in first and second scan) for the 410 W is 1.16°.

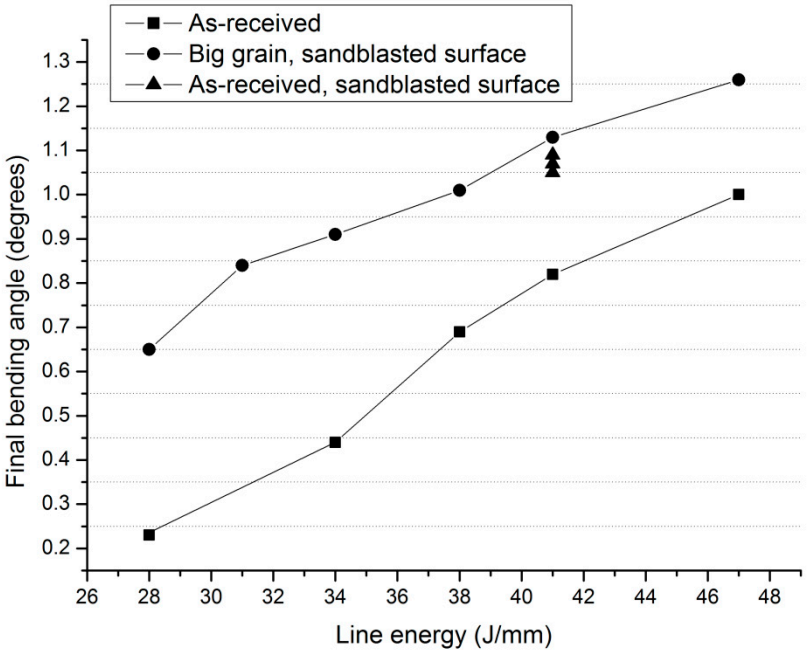

Figure 7. Bending angle response comparison for the CP Ti grade 2 samples which is: as-received, as-received with sandblasted surface and sandblasted surface with grown grains. The bending response is measured at different laser powers, with a fixed 15 mm/s transverse speed for all.

Figure 8 shows the [100] inverse pole figure (IPF) together with kernel average misorientation (KAM) maps for three laser powers (560 W, 720 W and 1000 W) which were subjected to the same scanning speed of 20 mm/s. Only alpha titanium has been detected inside LHAZ, similarly as in [21],

where welding of CP Ti by laser has been studied. These IFP maps show grain directions parallel to the plate surface normal in a central part of the laser track (top) and under the LHAZ area (bottom). The microstructural changes within the LHAZ (starting from the top towards the bottom) are evident and similar to that reported by [8] showing that these changes can be slip, grain fragmentation, recovery, grain boundary motion due to twinning, alpha-to-beta transformation, grain growth, phase transformation and recrystallization. The LHAZ in Figure 8 shows a fine-grained acicular alpha structure on the top of the LHAZ followed by columnar grains elongated in the direction perpendicular to the surface. This behaviour is seen throughout all the experiments. The depth of the columnar grains indicates the depth of the LHAZ, and this depth is shown in Figure 9 for all experiments mentioned in Table 1.

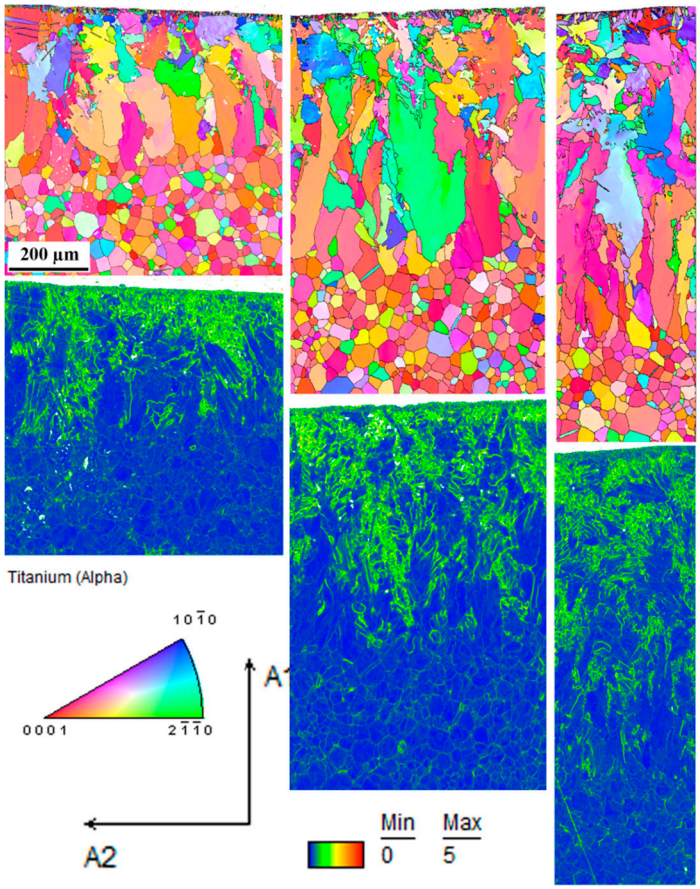

Figure 8. [100] inverse pole figure (IPF) (**top**) and kernel average misorientation (KAM) maps (**bottom**) of the 560 W (**left**), 720 W (**centre**) and 1000 W (**right**) scans with a scanning speed of 20 mm/s. The depth of the laser heat-affected zone (LHAZ) increases with an increase in laser power as indicated by the long columnar grains. No texture is observed after the forming process for all experimental results shown in Table 1. Scale bar 200 µm hold for all electron back-scatter diffraction (EBSD) maps in this figure.

One of the microstructural parameters studied involving transversal cross sections of laser tracks was the depth of LHAZ observed in the centre of the track. Figure 9 shows the relationship between the LHAZ depth and line energy. For a constant scanning speed the LHAZ increases approximately linearly with line energy. A higher scanning speed leads to a deeper LHAZ at constant line energy. These crystallographic findings of the LHAZ will be discussed in the following section dealing with EBSD.

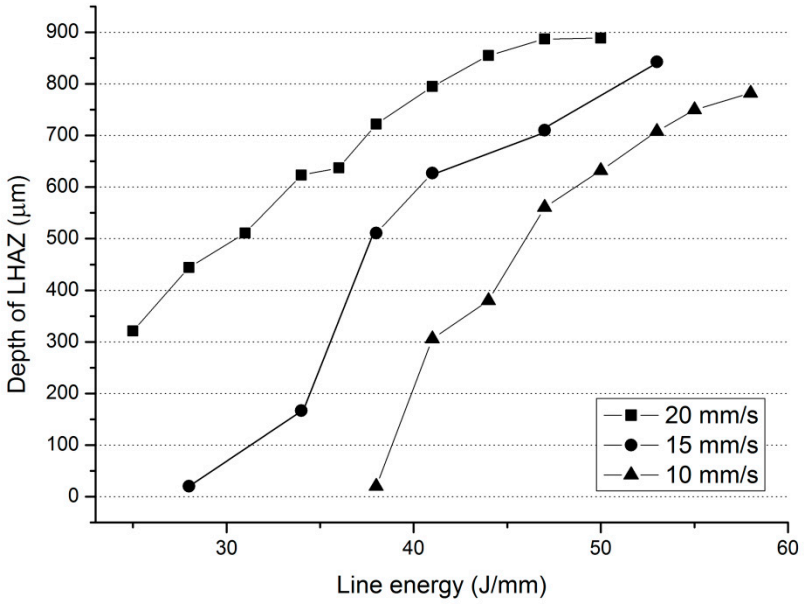

Figure 9. The depth of the LHAZ microstructure compared for different values of the laser parameters, power and transverse speed, with the maximum depth plotted against the line energy.

Figure 10 shows the [100] IPF and KAM maps for as-received, sandblasted, and large grain sandblasted sample tracks treated with the same laser power of 615 W and scanning speed of 15 mm/s. KAM is a well-established parameter to characterize local strain accumulated inside individual grains as described by [22]. For instance, the misorientation between a grain at the centre of the kernel and all points at the perimeter of the kernel are measured. The local misorientation value assigned to the centre point is the average of these misorientations. The graph on the bottom part of Figure 10 shows the averaged value of KAM for a particular LHAZ depth. The as-received KAM profile shows the highest accumulated strain at the surface with a gradual decrease within the LHAZ until ~550 µm. The sandblasted sample shows approximately the same strain near the surface, less steep decrease in depth, but a sharp decrease in KAM values from depths of ~650 to 700 µm. The large grain sand blasted sample shows a significant decrease in KAM values from the top (0 µm) to ~50 µm after which it increases to the values observed for other samples. Local strain shows again a sharp change over the boundary of the LHAZ. This sudden decrease leads to very fine first order pyramidal <C+A> slip planes that emerged during the high temperature deformation. The same pyramidal slip was detected as a main mechanism for producing elongation and shortening in the *c*-axis direction as reported by [23]. The depth of LHAZ is the smallest for the as-received sample without sandblasting, followed by the sandblasted sample and the largest for the large grain sandblasted sample.

The image quality (IQ) map shown in Figure 11 illustrates a general response of the microstructure with depth after the LF process which is observed in all LF samples listed in Table 1. For this LF sample (560 W, 20 mm/s), the first 10–20 µm (Region 1 in Figure 11) from the top shows a fine columnar microstructure followed by distorted grains that contain tensile and compression twining (Region 2). Region 3 gives rise to elongated columnar grain growth towards the centre which indicates that phase transformation occurred until this depth. The latter phenomenon is elaborated in the discussion. Region 4 is an unaffected substrate material throughout the rest of the sample. The grain boundaries can be defined as irregular sized, jagged and interlocking with each other.

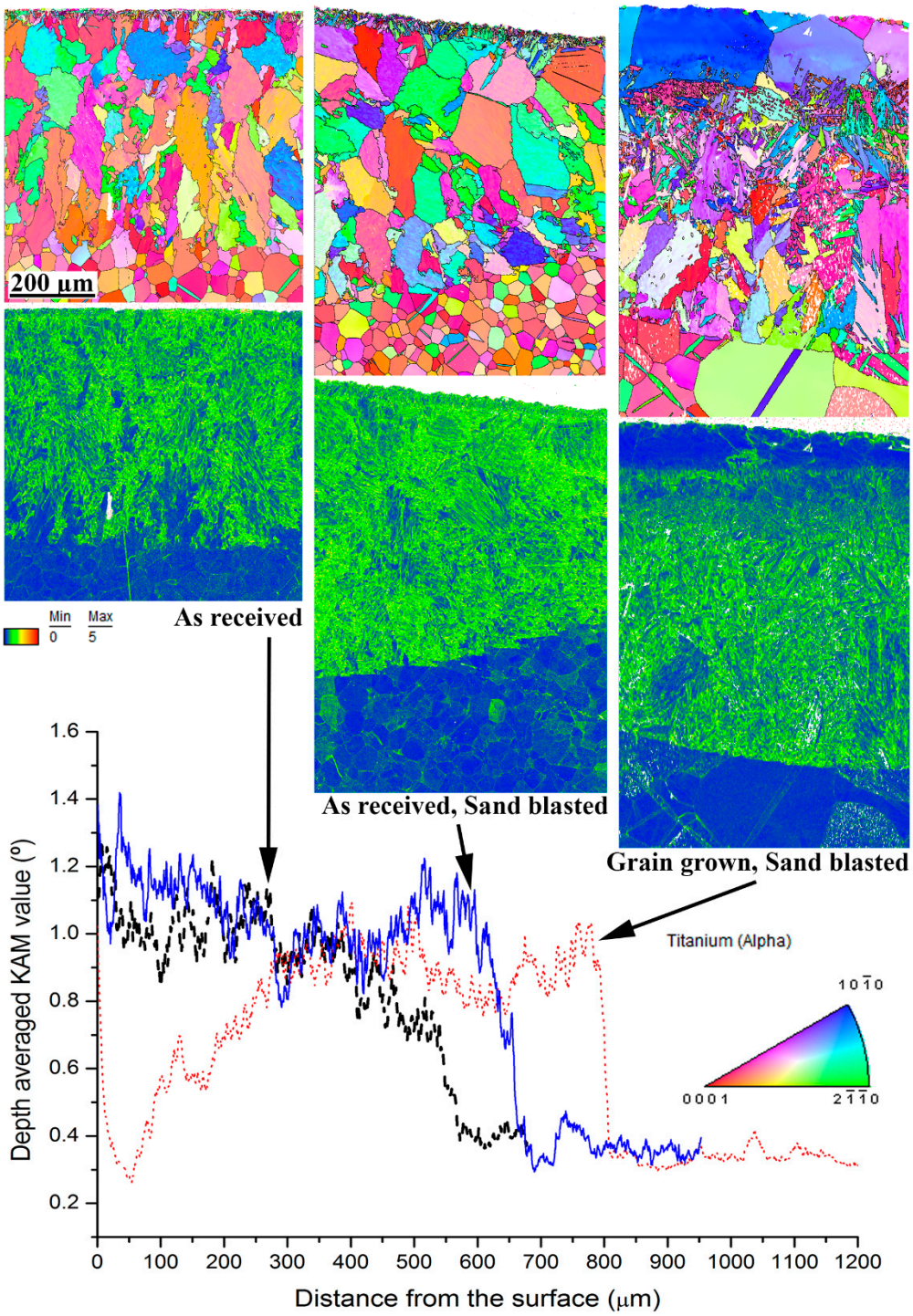

Figure 10. [100] IPF and KAM maps of the central parts of the laser track transversal cross-sections for as-received (**left**), sandblasted (**centre**) and large grain sandblasted (**right**) sample treated at 615 W and 15 mm scanning speed. Average KAM value profiles from the top surface to bottom under the LHAZ (**bottom**). Scale bar 200 µm hold for all EBSD maps in this figure.

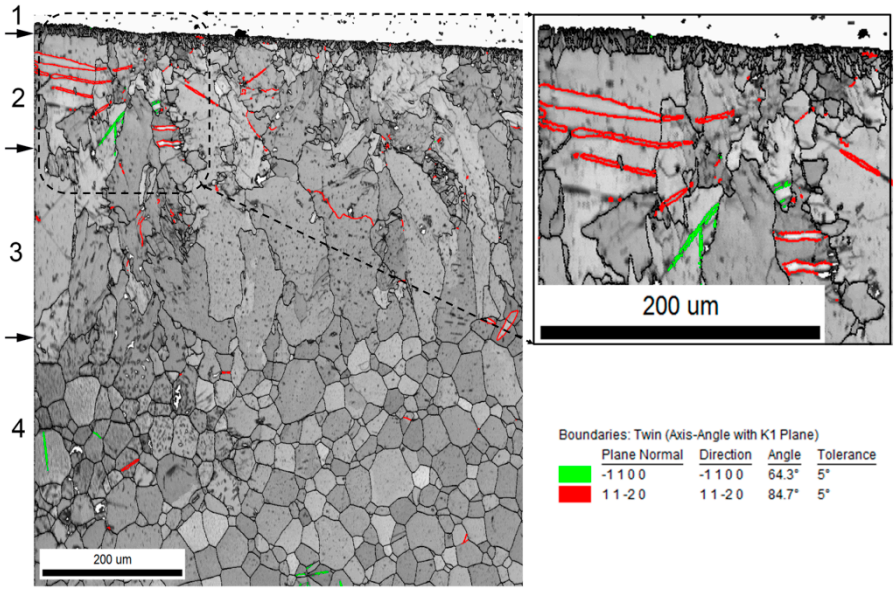

Figure 11. Image quality (IQ) maps with highlighted twins and small misorientation of the cross-section of the 560 W and 20 mm/s track. The image shows four regions that are similar for all of the as-received samples that were laser formed, namely, 1—fine microstructure at the top, 2—twining with distorted grains, 3—elongated columnar grain growth towards the centre, 4—unaffected substrate material.

4. Discussion

One would expect that the effect of the non-heated part of the bending line that is given stronger resistance to the bending operation may be a reason for an accelerated bending. As the laser makes progress over the sample, the non-heated (yet to be bent) part gets smaller and thus the resistance to bending is reduced. As already discussed in Section 3, the experimental results involving the bending of the plate as a whole showed no differences in the bending angle behaviour for line 2, 3, 4 and 5 (refer to Figure 2). Moreover, if the accelerated mechanism would be present then one would expect a bending angle acceleration during the entire LF process. Because this acceleration occurs only at the end (region 2–3, Figure 3) this must be associated with a temperature increase only because of the decreasing cooling ability near the sample edge.

As mentioned previously, the primary processing factors in laser forming are laser power, scanning speed and plate thickness. In is indicated in [3] that in the fields of welding and flame heating the parameters $\frac{P}{t\sqrt{v}}$ or $\frac{P}{\sqrt{v}}$ are used as the dependent parameter(s) to analyse the process variable effects on the bending angle. Results of the in situ laser forming observations summarized in Figure 5 clearly demonstrate that the final bending angle in LF of 3-mm thick Ti plates cannot be represented by a single linear least square fit because of the significant scatter in the data points represented by the different scanning speeds when the final bending angle is plotted against $\frac{P}{v}$. Replacing the line energy with the parameter $\frac{P}{\sqrt{v}}$ in Figure 5 results in the graph shown in Figure 12. The final bending angle data for the as-received sample surface results in a narrower band for all three scanning speeds. A linear fit over all data points in Figure 12 yields a reasonable estimation of the predicted bending angle as a function of laser power and scanning speed in agreement with a rather simple model proposed earlier [5]. The linear relationship is given by

$$\text{Bending angle} = 0.009\left(\frac{P}{\sqrt{v}}\right) - 0.632 \tag{4}$$

with a R^2 value equal to 0.8986. The preference for using $\frac{P}{\sqrt{v}}$ as the dependent variable in Equation (4) instead of $\frac{P}{v}$ is that Equation (4) can be used to calculate the final bending angle of 3-mm thick CP Ti

with laser scanning speeds ranging between 10 and 20 mm/s. The standard deviation of residuals from the linear fit in Figure 12 is approximately 18% which is a significantly closer prediction than what was previously reported by [4] in their Figure 2 which range between 45% and 100%.

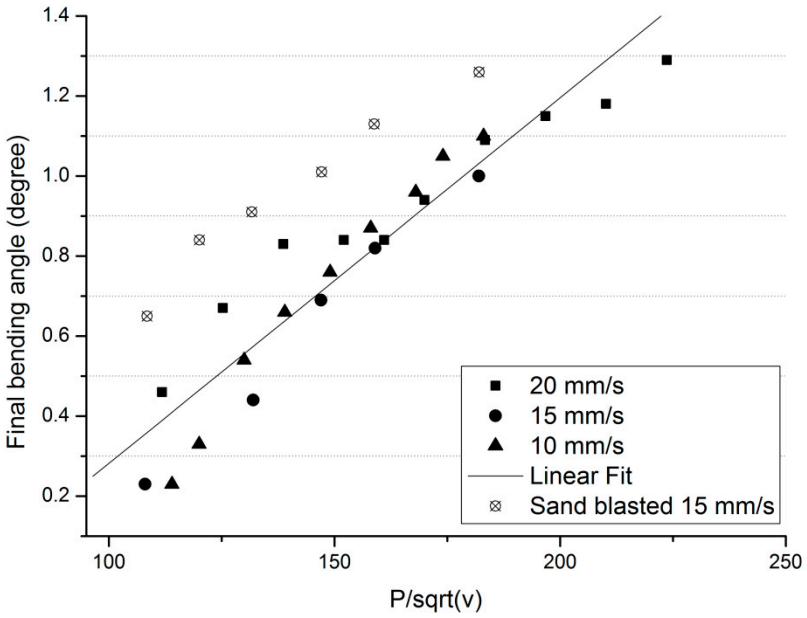

Figure 12. Final bending angle versus $\frac{P}{\sqrt{v}}$ parameter for 20, 15 and 10 mm/s, single scanned track on CP Ti.

It should be emphasized that the impetus for using the square root instead of the linear dependence on velocity was not purely a scientific one based on the physical reasoning but rather to propose an equation to predict an estimated value for the final bending angle.

Nevertheless, it is noteworthy that based on qualitative physical arguments a square root instead of a linear dependence on velocity can be expected by realizing that the bending phenomenon appears due to a stress gradient. Taking linear elasticity as a starting point, a stress gradient $\partial\sigma$ can be converted to a gradient in thermal strain $\partial\varepsilon$ as a result of a temperature gradient ∂T. As a consequence the temperature gradient can be written as the product of heat density input, i.e., the heat input per unit of area, and the heat resistance, which is nothing else than the thermal diffusion length l over the thermal conductivity λ_t, i.e., a higher thermal conductivity means a lower heat resistance. Taking phonons as the crucial carriers of heat transport in metallic systems the thermal diffusion length is, in a first approximation, proportional to the square root of the product of thermal diffusivity and interaction/dwell time τ involved. The latter is inversely proportional to the laser beam velocity v_l, i.e., the bending angle α_b becomes inversely proportional with the square root of the v_l, i.e.,

$$\alpha_b \propto \partial\sigma \propto \partial\varepsilon \propto \partial T \propto \frac{l}{\lambda_t} \propto \sqrt{\tau} \propto \frac{1}{\sqrt{v_l}} \tag{5}$$

So, in summary a square root dependence of bending angle and laser beam velocity looks physically sound. Of course, details of the temperature field of a moving heat source matter and can be described in a more sophisticated way based on solving the differential equations of heat conduction using various mathematical frameworks [24–26], but that is not the purpose of this paper.

In addition, it should be noted that the results of this study are purely based on CP Ti, whereas different materials (i.e., other than CP Ti) are considered in Figure 2 of [4]. The significantly larger error range reported by [4] may be due to the fact that more parameters (each subject to its own percentage error range) are involved in their equations for the bending angle (given by

Equations (1) and (2) in this study). When plotting the final bending angle of the as-received and the grain grown sandblasted sample on the same graph (open symbols in Figure 12), it is evident that the trend of the sandblasted sample follows a linear fit similar to that of the as-received samples, however, it is shifted to the higher values because of the increase in the energy absorption coefficient caused by sandblasting. Nevertheless, the influence of plate thickness has to be further investigated, since in the current experiment a thickness of only 3-mm was used, but this falls beyond the scope of the current study.

It should be noted that for multiple overlapping tracks the bending angle per track from the second to sixth track slowly decreases to an almost constant bending angle per track. This could be attributed to a build-up of residual stresses in the LHAZ since it has been previously reported by [17] that the relieved residual stresses can be as high as 108 MPa after the sixth scan. The fact that the bending angle between the first and the second laser scan increased between 5% and 24% can be attributed to the change in surface absorptivity after the first track passes the surface when moving from the first to the second track.

For an in-depth understanding of the heat flow within the material a 3D time dependent FEM is generated using COMSOL Multiphysics. An example of the iso-surface plot for the track processed with a laser power of 440 W and a speed of 10 mm/s is presented in Figure 13. The heat transfer during the laser forming process, when the beam is located in the middle of the track length is illustrated. The area for the high temperature isolines stay roughly circular, however, during the conduction of heat the isothermal lines become egg shaped because of the movement of the laser on the surface.

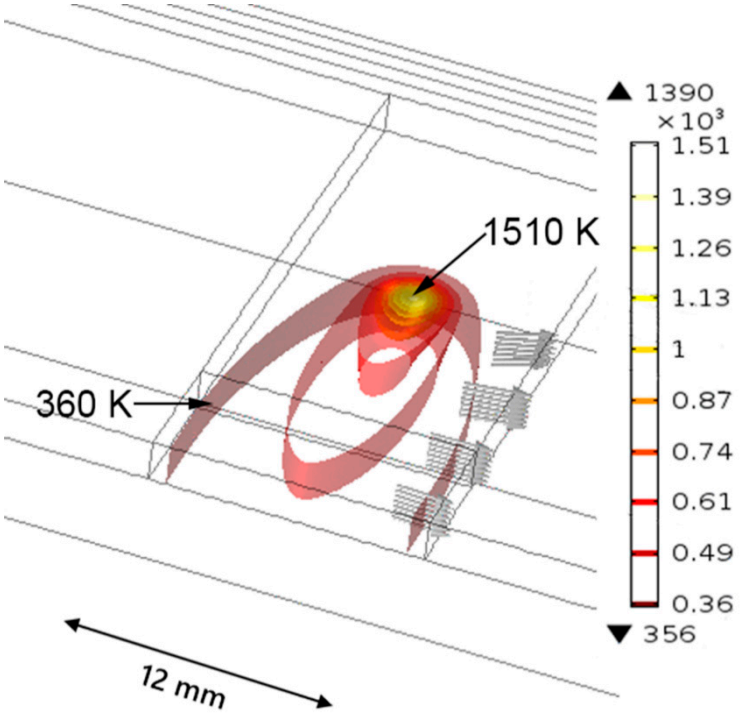

Figure 13. A 3D iso-surface temperate plot (in Kelvin) of the laser beam heat model, showing iso-surfaces of different temperatures. The arrows represent the direction of the heat flux.

Furthermore, the maximum temperature value is almost constant as the laser beam moves over the plate, until the laser beam approaches the edge where the maximum temperature rises causing the previously mentioned edge effect. For example, using parameters of 720 W and 20 mm/s, the maximum temperature at the position shortly behind the beam centre rises from 1390 K in the centre of the track length to 1540 K at the edge of the sample as shown in Figure 14 by the dashed line. This FEM allows calculation of the temperature history at any point inside the plate. By highlighting the

temperature range of the α to β phase transformation in the graph where the maximum temperature is plotted as a function of depth for different combinations of processing parameters (Figure 14), an expected depth of the phase change can be estimated. These estimated depths are almost identical to the experimentally measured depths of the LHAZ microstructure, as shown in Figure 9. Although the experimental data was used to calibrate the FEM and the FEM was used to determine the dependence of the maximum temperature on the depth of the sample for different laser power and scanning speeds, it should be noted that the FEA was used as primary purpose of serving as supporting tool in order to understand the underlying physical phenomena of the laser process and not as an exact measure for validating the results obtained with the laser scanning speed. Similar results for the sample depth have been reported by [8] in which only an approximate equation for heat transfer in titanium has been used. Therefore it can be concluded that the size of the LHAZ observed by EBSD is identical to the volume undergoing phase transformation.

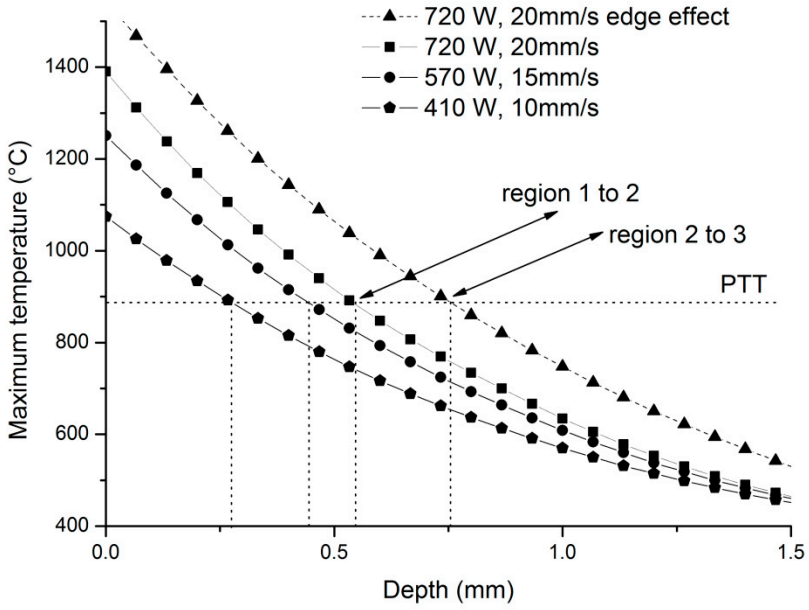

Figure 14. Maximum temperature achieved in the points under track centre plotted against their distance from the surface (depth) calculated from the FEM. The α to β phase transformation temperature (PTT) is highlighted and the depth in which transformation occurs is estimated by vertical dashed lines. A difference between the phase transformation depth at the centre of the laser track (bending with slow rate, region 1 to 2 in Figures 3 and 4) and on the edge of the plate (accelerated bending, region 2 to 3 in Figures 3 and 4) is also shown.

By extrapolating the abovementioned model, one can determine a relationship between the laser power, scanning speed and maximum surface temperature. The results shown in Figure 15 are a set of maximum surface temperatures of 1325 K, 1546 K and 1734 K with respect to a varying scanning speed (5 to 25 mm/s).

A correlation of the bending angle and depth of LHAZ is observed when comparing Figure 9 to Figure 14. Detected local strain by KAM reveals that the amount of the (peak) local strain is not substantially different between the as-received and sandblasted specimens, although, the depth of local strain increased. Furthermore, the actual size of the transformed microstructure volume (indicated by the KAM) determines the size of the bending angle. This increase in KAM depth from the surface varied between approximately 20 to 38%. It was also established that the LHAZ boundary is in agreement with the depth of the α to β phase transformation line determined by the FEM. In Figure 15 it is shown that the maximum temperature achieved depends on the scanning speed and the laser power. Three isotherm curves are shown which illustrate that in order to achieve a phase transformation temperature

at some particular depth with an increase in scanning speed it is necessary to increase the laser power proportional to $\sqrt{v}$. This is illustrated by the inserted figure on the top left-hand side of Figure 15.

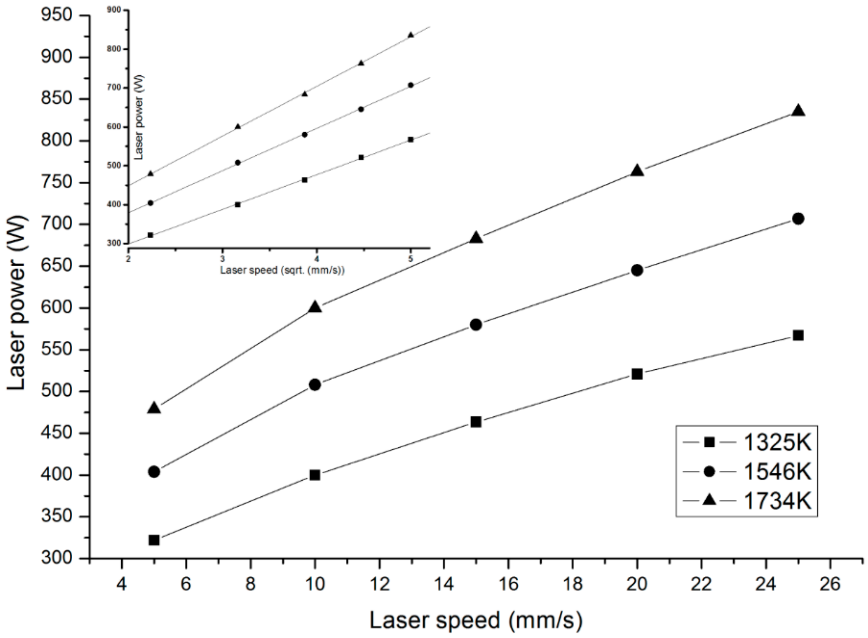

Figure 15. The laser power plotted against the laser scanning speed for three maximum surface temperatures. The inserted figure on the top left-hand side represents the laser power versus square root of the laser scanning speed with a linear regression indicated for each maximum surface temperature.

It is known that sandblasting could substantially influence the amount of absorbed laser energy. Therefore the size of the transformed volume also changes substantially and this is the reason why the bending angle was significantly increased for samples after sandblasting. On the other hand, the grain size could affect the size of the transformed area mostly via a change in thermal conductivity, but the effect is much smaller in comparison with a change in absorption after sandblasting (as shown in Figure 7).

5. Summary and Conclusions

A correlative comparison is presented between laser forming parameters and microstructural changes by utilizing in situ digital image correlation and electron backscatter diffraction techniques. Digital image correlation revealed that the final bending response is uniform over the entire plate width and no torsional effects can be observed when using a 3-mm thick commercially pure titanium sample. The behaviour of the material because of the laser forming process may offer the industry relevant information when considering advanced forming methods. The conclusions are summarized as follows:

1 The bending rate during the laser forming process is constant and increases as the laser beam moves over the final plate edge. For multiple overlapping tracks the final bending angle per track varies for each of the processing parameters (laser power and scanning speed) but decreases slightly to an asymptotic value.

2 The final bending angle of a thick Ti plate scales with the ratio $\frac{P}{\sqrt{v}}$ where P represents the laser power and v is the laser beam scanning speed. However, surface roughness and therefore different absorptivity substantially influences the final bending angle. The scaling of the final bending angle with $\frac{P}{\sqrt{v}}$ in the figures provided for the final bending angle as opposed to $\frac{P}{v}$ has been justified by relating the direct proportionality of the bending angle to the temperature gradient.

3 The local strain by KAM suggests that the amplitude of local strain does not depend critically on the processing conditions. However, the total strain increases with the depth of the LHAZ. Both deformation mechanisms (dislocation slip and twinning) are detected. However sandblasted samples with large grains show a high degree of pyramidal first-order <C+A> slip near the treated surface.

Specifically for relatively thick (3 mm) Ti plate and the range of laser processing parameters used, the actual size of the volume of the transformed microstructure determines the magnitude of the bending angle. FEM showed agreement between the phase transformation depth and the microstructurally determined size of the LHAZ. Experimental observations also prove that the depth of the LHAZ scales with $\frac{P}{\sqrt{v}}$ rather than with $\frac{P}{v}$, similarly as the final bending angle.

Author Contributions: H.F. and V.O. conceived and designed the experiments. H.F., J.P.J.A. and V.O. performed the experiments. H.F., J.P.J.A., V.O. and J.T.M.D.H. contributed to the data analysis and scientific interpretation of the work. H.F. drafted the article. H.F., V.O. and J.T.M.D.H. made critical revisions to the article. All authors have read and agreed to the published version of the manuscript.

Funding: This research received no external funding.

Acknowledgments: The work was supported by the Applied Physics-Materials Science group of the Zernike Institute for Advanced Materials of the University of Groningen, The Netherlands.

Conflicts of Interest: The authors declare no conflict of interest.

References

1. Namba, Y. Laser Forming of Metals and Alloys. In Proceedings of the LAMP'87, Osaka, Japan, 21–23 May 1987; pp. 601–606.
2. Scully, K. Laser Line Heating. *J. Ship Prod.* **1987**, *3*, 237–246.
3. Vollersten, F. Mechanisms and Models for Laser Forming. In Proceedings of the Laser Assisted Net Shape Engineering Conference, Bamberg, Germany, 12–14 October 1994; pp. 345–359.
4. Shen, H.; Vollertsen, F. Modelling of laser forming—An review. *Comput. Mater. Sci.* **2009**, *46*, 834–840. [CrossRef]
5. Geiger, M.; Vollertsen, F. The Mechanisms of Laser Forming. *CIRP Ann.* **1993**, *42*, 301–304. [CrossRef]
6. Geiger, M.; Merklein, M.; Pitz, M. Laser and forming technology—An idea and the way of implementation. *J. Mater. Process. Technol.* **2004**, *151*, 3–11. [CrossRef]
7. Els-Botes, A.; Fidder, H.; Woudberg, S.; McGrath, P.J. Mechanical Characterisation of the Effect of Various Forming Processes Applied to Commercially Pure Titanium. *Mater. Charact.* **2014**, *96*, 206–212. [CrossRef]
8. Fidder, H.; Ocelík, V.; Botes, A.; De Hosson, J.T.M. Response of Ti microstructure in mechanical and laser forming processes. *J. Mater. Sci.* **2018**, *53*, 14713–14728. [CrossRef] [PubMed]
9. Shi, Y.; Zhang, C.; Sun, G.; Li, C. Study on reducing edge effects by using assistant force in laser forming. *J. Mater. Process. Technol.* **2016**, *227*, 169–177. [CrossRef]
10. Safari, M.; Farzin, M. Experimental investigation of laser forming of a saddle shape with spiral irradiating scheme. *Opt. Laser Technol.* **2015**, *66*, 146–150. [CrossRef]
11. Chakraborty, S.S.; More, H.; Nath, A.K. Laser forming of a bowl shaped surface with a stationary laser beam. *Opt. Lasers Eng.* **2016**, *77*, 126–136. [CrossRef]
12. Maji, K.; Pratihar, D.K.; Nath, A.K. Experimental investigations, modeling, and optimization of multi-scan laser forming of AISI 304 stainless steel sheet. *Int. J. Adv. Manuf. Technol.* **2016**, *83*, 1441–1455. [CrossRef]
13. Vollertsen, F.; Komel, I.; Kals, R. The laser bending of steel foils for microparts by the buckling mechanism—A model. *Model. Simul. Mater. Sci. Eng.* **1995**, *3*, 107. [CrossRef]
14. Yau, C.L. A New Analytical Model for Laser Bending. Laser Assisted Net Shape Engineering 2. In Proceedings of the LANE'97, Erlangen, Germany, 23–26 September 1997; pp. 357–366.
15. Chu, T.C.; Ranson, W.F.; Sutton, M.A. Applications of digital-image-correlation techniques to experimental mechanics. *Exp. Mech.* **1985**, *25*, 232–244. [CrossRef]
16. Pretorius, T.; Habedank, G.; Woitschig, J.; Vollertsen, F. Thermal Generation of Residual Stress Fields for Purpose of Distortion Minimization. *Materialwissenschaft und Werkstofftechnik* **2006**, *37*, 85–91. [CrossRef]

17. Fidder, H.; Els-Botes, A.; Woudberg, S.; McGrath, P.J.; Ocelik, V.; de Hosson, J.T.M. A study of microstructural fatigue and residual stress evolution in titanium plates deformed by mechanical and laser bending. In *Surface Effects and Contact Mechanics Including Tribology*; De Hosson, J.T.M., Hadfield, M., Brebbia, C.A., Eds.; WIT Press: Southampton, UK, 2005; pp. 23–34.
18. Basu, I.; Fidder, H.; Ocelík, V.; Th M de Hosson, J. Local Stress States and Microstructural Damage Response Associated with Deformation Twins in Hexagonal Close Packed Metals. *Crystals* **2018**, *8*, 1. [CrossRef]
19. Hennige, T. Development of irradiation strategies for 3D-laser forming. *J. Mater. Process. Technol.* **2000**, *103*, 102–108. [CrossRef]
20. Li, W.; Yao, Y.L. Laser Forming with Constant Line Energy. *AMT* **2001**, *17*, 196–203. [CrossRef]
21. Li, C.; Muneharua, K.; Takao, S.; Kouji, H. Fiber laser-GMA hybrid welding of commercially pure titanium. *Mater. Des.* **2009**, *30*, 109–114. [CrossRef]
22. Wright, S.I.; Nowell, M.M.; Field, D.P. A Review of Strain Analysis Using Electron Backscatter Diffraction. *Microsc. Microanal.* **2011**, *17*, 316–329. [CrossRef] [PubMed]
23. Zeng, Z.; Zhang, Y.; Jonsson, S. Deformation behaviour of commercially pure titanium during simple hot compression. *Mater. Des.* **2009**, *30*, 3105–3111. [CrossRef]
24. Carslaw, H.S.; Jaeger, J.C. *Conduction of Heat in Solids*; Clarendon Press: London, UK, 1959.
25. Beck, J.V.; Cole, K.D.; Haji-Sheikh, A.; Litkouhi, B. *Heat Conduction Using Green's Function*; Taylor & Francis: New York, NY, USA, 1992; ISBN 978-0-429-25836-7.
26. Özısık, M.N. *Heat Conduction*; John Wiley & Sons: New York, NY, USA, 1993.